Imaging and modeling the ionospheric airglow response over Hawaii to the tsunami generated by the Tohoku Earthquake of 11 March 2011

J. J. Makela,[1] P. Lognonné,[2] H. Hébert,[3] T. Gehrels,[1] L. Rolland,[2] S. Allgeyer,[3] A. Kherani,[4] G. Occhipinti,[2] E. Astafyeva,[2] P. Coïsson,[2] A. Loevenbruck,[3] E. Clévédé,[2] M. C. Kelley,[5] J. Lamouroux[6]

S. Allgeyer, H. Hébert, A. Loevenbruck, CEA-DAM-DIF, F-91297 Arpajon, France.

E. Astafyeva, E. Clévédé, P. Coïsson, P. Lognonné, G. Occhipinti, L. Rolland, Institut de Physique du Globe de Paris, Sorbonne Paris Cité, Univ. Paris Diderot, UMR 7154 CNRS, F-94100 Saint Maur des Fossés, France.

T. Gehrels, J. J. Makela, Department of Electrical and Computer Engineering, University of Illinois at Urbana-Champaign, Urbana, Illinois 61822, USA. (jmakela@illinois.edu)

M. C. Kelley, School of Electrical and Computer Engineering, Cornell University, Ithaca, New York, USA.

A. Kherani, Instituto Nacional de Pesquisais Espaciais (INPE), Sao Jose dos Campos, Sao Paula, BR-12227010, Brazil.

J. Lamouroux, NOVELTIS, Parc Technologique du Canal, 2, Avenue de l'Europe, F-31520 Ramonville-Saint-Agne, France.

[1]Department of Electrical and Computer

Although only centimeters in amplitude over the open ocean, tsunamis can generate appreciable wave amplitudes in the upper atmosphere, including the naturally occurring chemiluminescent airglow layers, due to the exponential decrease in density with altitude. Here, we present the first observation of the airglow tsunami signature, resulting from the 11 March 2011 Tohoku earthquake off the eastern coast of Japan. These images are taken using a wide-angle camera system located at the top of the Haleakala Vol-

Engineering, University of Illinois at Urbana-Champaign, Urbana, Illinois, USA.

[2]Institut de Physique du Globe de Paris, Sorbonne Paris Cité, Université Paris Diderot, France.

[3]CEA-DAM-DIF, Arpajon, France.

[4]Instituto Nacional de Pesquisais Espaciais (INPE), Sao Jose dos Campos, Sao Paula, Brazil.

[5]School of Electrical and Computer Engineering, Cornell University, Ithaca, New York, USA.

[6]NOVELTIS, Ramonville-Saint-Agne, France.

cano on Maui, Hawaii. They are correlated with GPS measurements of the total electron content from Hawaii GPS stations and the Jason-1 satellite. We find waves propagating in the airglow layer from the direction of the earthquake epicenter with a velocity that matches that of the ocean tsunami. The first ionospheric signature precedes the modeled ocean tsunami generated by the main shock by approximately one hour. These results demonstrate the utility of monitoring the Earths airglow layers for tsunami detection and early warning.

1. Introduction

As a tsunami propagates over the open ocean, atmospheric gravity waves (AGWs) forced by the centimeter-level surface undulations are generated [*Hines*, 1960; *Peltier and Hines*, 1976]. Due to the decrease in atmospheric density and the requirement that wave momentum is conserved, the amplitudes of the forced AGWs can reach several kilometers at altitudes where the neutral atmosphere coexists with the plasma in the ionosphere ($\sim$ 250 km), perturbing the ionosphere through collisions between the neutrals and the charged particles [*Occhipinti et al.*, 2008; *Hickey et al.*, 2009]. This ionospheric response was originally conjectured in the 1970s and formed the basis of a proposed tsunami early detection technique [*Najita et al.*, 1974]. In the intervening decades, little progress was made in utilizing any ionospheric observation methods due to the relative paucity of required measurements.

The first observation using the very dense Japanese GPS Earth Observation Network (GEONET) was reported in 2005, with the imaging of the ionospheric perturbations related to the trans-Pacific tsunami generated by the Mw=8.2 earthquake that occurred in Peru on 23 June 2001 [*Artru et al.*, 2005]. Additionally, several observations were performed during the 2004 Sumatra tsunami. These observations rely on estimates of the total electron content (TEC), the integrated electron density between a specific GPS satellite and receiver [*Liu et al.*, 2006; *Lognonné et al.*, 2006] or between a satellite-based altimeter and the sea surface, and have been numerically reproduced [*Occhipinti et al.*, 2006]. Subsequent studies have shown systematic ionospheric tsunami detection utilizing GPS-derived TEC was possible using smaller networks, such as on Hawaii [*Rolland*

et al., 2010]. However, as the density and coverage of the available GPS network decrease, the ability to "image" the ionospheric response is lost. Furthermore, the ability to detect the tsunami is dependent on the constantly changing geometry of the GPS satellite constellation in addition to the background ionospheric structure.

Here and for the first time, we utilize a highly sensitive, wide-angle camera system to image the tsunami-driven ionospheric response to the 11 March 2011 Tohoku earthquake. From a single instrument located on the Haleakala Volcano on Maui, Hawaii, we are able to image a 10^6 km^2 region of the ionosphere at high spatial ($\sim 1-5$ km, elevation angle dependent) and temporal (~ 5 min) resolutions. This is done by observing the airglow layer at approximately 250 km in altitude caused by the dissociative recombination of O_2^+ [*Link and Cogger*, 1988], which emits photons at 630.0 nm. Modeling studies have suggested that appreciable modulations in the 630.0-nm intensity should be caused by tsunami-driven AGWs [*Hickey et al.*, 2010]. However, until now, this has never been demonstrated.

2. Data Presentation and Analysis

As reported by the United States Geological Survey (USGS), the Mw=9.0 Tohoku earthquake occurred at 05:46:23 UT off the east coast of Honshu, Japan (38.322° N, 142.369° E). Based on the measurement of the Deep-ocean Assessment and Reporting of Tsunamis (DART) buoy 51407 located near the Big Island of Hawaii (19.6° N, 203.5° E), the arrival of the tsunami was predicted at 13:07 (PTWC message 5) and the first maximum amplitude (15 cm) is reported at 13:37 UT (PTWC message 27). Tsunami Travel Time software [*Wessel*, 2009] using the USGS seismic source predicts an arrival

time of 13:17 UT at the DART 51407. The imaging system utilized in this study began routine observations at 10:32 UT and continued observing until 15:19 UT. The skies were predominately clear, with only a few low-lying clouds observed over the course of the night and we can therefore be confident structures observed are actually in the airglow layer.

Initial analysis of the raw images collected of the 630.0-nm emission on this night exhibited little of interest related to the tsunami. Typical structures observed in this imaging system can include north-south aligned and eastward propagating equatorial plasma bubbles [e.g., *Kelley et al.*, 2002; *Makela et al.*, 2004], northwest-southeast aligned and southwestward propagating medium-scale traveling ionospheric disturbances [MSTID; e.g., *Makela et al.*, 2009; *Miller et al.*, 2009], and poleward propagating brightness waves. A very faint MSTID is observed from the beginning of the observations until approximately 11:30 UT (much earlier than the expected tsunami arrival time) and a distinct brightness wave is observed from 12:45-13:45 UT. Neither of these features are tsunami related.

A more detailed analysis was performed in which the images were projected onto an assumed emission layer altitude of 250 km and then passed through a filter to isolate specific wave periods. Three different length-8 FIR filters were used with passbands of 0.3-1.0 mHz, 1.0-1.7 mHz, and 0.3-1.7 mHz. The imaging data were sampled at approximately 3.6 mHz. A Gabor filter was then used to estimate the spatial frequency and propagation angle of waves within each passband. This filtering revealed both a long-period wave ($T = 26.2 \pm 3.1$ min; $\lambda = 290.0 \pm 12.5$ km; $v = 184.5 \pm 33.8$ m/s) and a short-period wave ($T = 14.2 \pm 2.7$ min; $\lambda = 189.9 \pm 4.9$ km; $v = 222.9 \pm 52.4$ m/s) propagating in the

direction of the tsunami as it passed by the Hawaiian Islands. Example filtered images are shown in Figure 1 and a movie showing all of the filtered images collected on this night is included in auxiliary online material.

The long- and short-period waves have slightly different arrival directions ($132^\circ \pm 1^\circ$ and $136^\circ \pm 1^\circ$ azimuth, respectively) before approximately 13 UT, suggesting that the source of these two wave packets may be different. However, ray tracing of the tsunami (not shown) indicates that the two azimuths reported for the ionospheric early waves originate from the rupture zone reported by USGS. This focusing can be attributed to the Hawaiian-Emperor seamount chain bathymetry, which acts as a tsunami waveguide. After approximately 13 UT, both waves show an arrival direction of $134^\circ \pm 1^\circ$. The alignment and propagation direction of the observed waves is inconsistent with the other types of structures typically seen in this imaging system and their occurrence at the same time, direction, and speed as the tsunami makes it reasonable to attribute these airglow waves to the tsunami propagation.

To confirm this hypothesis, we have obtained GPS 30-sec sampled data from 52 receivers on the Hawaiian Islands available on the UNAVCO public ftp website (ftp://data-out.unavco.org/). Following the methodology of [*Rolland et al.*, 2010], we have extracted the tsunami signature in these data. Similarly, we have obtained TEC data measured with the dual-frequency altimeter on the Jason-1 satellite and have extracted the tsunami signature as done previously for the Sumatra tsunami [*Occhipinti et al.*, 2006]. We have compared these measurements to the imaging data collected on this night and the waves

seen in the TEC data are collocated in space and time with the waves observed in the images, as shown in the movie.

Time of arrival diagrams constructed using the airglow data and GPS-derived TEC data are presented in Figure 2. In this representation, structures that are moving with the tsunami (in terms of both direction and speed) appear as vertical bands. Structures arriving before the tsunami appear at negative time values on the x axis, while structures following the tsunami appear at positive time values. It is evident from this figure that structures are seen in the ionosphere approximately one hour ahead of the tsunami.

3. Discussion

The observed early waves, if indeed related to the earthquake, may have several competing origins. They might be caused by (a) an infrasonic wave generated at the earthquake source propagating in the ionosphere faster than the ocean tsunami wave front, (b) a plasma diffusion oscillation related to the sea-level disturbances of the tsunami wave front, or (c) the initial tsunami wave generated by a pre-rupture processes.

If the observed early waves were caused by an infrasonic wave generated at the earthquake source and traveling in the ionosphere, we would expect them to be observed propagating from the geometrical direction between the source region and Hawaii. This would be an azimuth angle of approximately 123° which differs significantly from the observed azimuth angles. Secondly, if this were the case, we would not expect to see any associated early perturbations at the ocean surface which, as shown below, are observed. Neither such an infrasonic wave nor the ocean floor deformation generated by the tsunami loading can generate the observed waves.

125 To examine the second potential cause of these early waves, we use a sea-level modeling
126 of the tsunami as generated following the methodology of *Hébert et al.* [2007] and using
127 the USGS finite fault model (provided at http://earthquake.usgs.gov/earthquakes) for
128 the Tohoku earthquake. We model the resultant AGWs and associated ionospheric waves
129 with two different methods, assuming either a pure gravity wave regime [*Occhipinti et al.*,
130 2006, 2008] or a gravity-acoustic regime [*Kherani et al.*, 2009]. A comparison of the
131 observed ionospheric waves in the airglow and each model's response at 250 km (the
132 altitude of the assumed peak in the airglow intensity) is presented in Figure 3. The
133 agreement between the observations of waves after the arrival of the tsunami and modeling
134 in both cases is not only conclusive in arrival time and wave structure azimuth, but also
135 for several features appearing in the wave structures [*Occhipinti et al.*, submitted, 2011],
136 which are observed about one hour after the passage of the tsunami. However, no evidence
137 of the early wave is seen in either model.

138 To test the third hypothesis, a closer analysis of the DART data has been performed.
139 The large tidal signature in the data was removed using the 45-day average tidal signature
140 from the DART measurements on 11 March 2011 using a least squares fitting process. The
141 raw data and the data with the tide removed in this way are presented in the top two
142 panels of Figure 4. The residual sea level measurement shows a 1-cm retreat preceded
143 by a slow ramp extending approximately 90 minutes before the arrival of the tsunami
144 at the DART buoy. Superposed on this ramp are higher-frequency waves. Additional,
145 independent methods for removing the tidal signature, including a high-pass filter and a
146 Fourier methodology, were performed and confirm the presence of the 1-cm retreat and

preceding ramp with superposed waves features, as shown in the third panel of Figure 4. A spectral analysis of the residual signal, presented in the bottom-right panel of Figure 4, indicates that the energy in these early waves has a dominant period of about 28 min with lesser contributions at shorter periods, which include the 14 min period. This suggests that the early waves observed in the ionosphere are related to these small oscillations seen on the ocean surface.

A model of the expected sea level variations, taking into account the characteristics of the fault source reported by the USGS, is presented as the red line in the second panel of Figure 4. A second, independent model of the expected sea level variations was also run following the method of [*Hébert et al.*, 2007], and is presented as the red line in the third panel of Figure 4. Neither modeling methodology generates the observed ramp and associated small fluctuations seen in the residual signal. Analysis of other DARTs (43412, 51406, 43413 and, with more noise, 52406 and 32413) indicate similar features. As our ocean-to-atmosphere modeling presented above, which relies on the sea-surface models, does not generate the observed early ionospheric waves and since the infrasound hypothesis would not generate such a sea level displacement, we conclude that a seismic origin for this early wave, possibly due to pre-rupture processes and not included in the USGS fault source, is likely.

As shown here, the use of an imaging system observing the airglow layers in the ionosphere provides a powerful tool for monitoring the passage of tsunamis. Dense networks of instruments are not required to produce an image, as is the case using GPS-derived TEC, and classical image processing techniques can be applied to enhance the utility of

the information derived from the measurements. However, the airglow technique does have its drawbacks. Specifically, the ground-based camera system utilized here is constrained to taking images when both the sun and the moon are below the local horizon and the skies overhead are clear, conditions that will not be met for every tsunami event. Furthermore, these types of systems are constrained to land-based locations making monitoring the entire Pacific Ocean, for example, impossible. However, an imaging system on a space-based platform would not suffer from these limitations. Several emissions sensitive to the ionospheric density are observable from space on both the night- and dayside, with the most promising being the far ultraviolet OI emission at 135.6 nm. The response of this emission to a tsunami-induced AGW has been modeled in *Hickey et al.* [2010]. A geostationary platform would allow for continual monitoring of large regions of the Earth and usher in a new era of tsunami monitoring.

Acknowledgments. Work at the University of Illinois was supported by the United States Office of Naval Research (ONR) through grant N00014-09-1-0439 and the National Science Foundation through grant ATM 06-44654 CAR. The French contribution of the project (IPGP contribution nxxxx) has been supported by the French Space Agency, CNES, by the PNTS program, and by ONR Global under contract IONONAMI-N07-25. Noveltis provided additional support for GPS/JASON TEC analysis software development. E. Clévédé thanks B.Bukchin for source inversion and P.Lognonné thanks T.Gabsi, K.Douch, M.Mann for data analysis and archiving effort. Work at Cornell University was supported by ONR. We thank, DART/NOAA, NASA, SOPAC, UNAVCO, GEOSCOPE

for data collection, J. Burger for his help operating the imaging system, and Dr. R. McCoy for fruitful discussions and bridging the US and French groups.

References

Artru, J., V. Ducic, H. Kanamori, P. Lognonné, and M. Murakami (2005), Ionospheric detection of gravity waves induced by tsunamis, *Geophys. J. Int.*, *160*(3), 840–848, doi:10.1111/j.1365-246X.2005.02552.x.

Hébert, H., A. Sladen, and F. Schindelé (2007), Numerical modeling of the great 2004 Indian Ocean tsunami: Focus on the Mascarene Islands, *B. Seismol. Soc. Am.*, *97*(1A), S208–S222, doi:10.1785/0120050611.

Hickey, M. P., G. Schubert, and R. L. Walterscheid (2009), Propagation of tsunami-driven gravity waves into the thermosphere and ionosphere, *J. Geophys. Res.*, *114*, A08304, doi:10.1029/2009JA014105.

Hickey, M. P., G. Schubert, and R. L. Walterscheid (2010), Atmospheric airglow fluctuations due to a tsunami-driven gravity wave disturbance, *J. Geophys. Res.*, *115*, A06308, doi:10.1029/2009JA014977.

Hines, C. O. (1960), Internal atmospheric gravity waves at ionospheric heights, *Can. J. Phys.*, *38*(11), 1441–1481.

Kelley, M. C., J. J. Makela, B. M. Ledvina, and P. M. Kintner (2002), Observations of equatorial spread-F from Haleakala, Hawaii, *Geophys. Res. Lett.*, *29*(20), 2003, doi: 10.1029/2002GL015509.

Kherani, E. A., P. Lognonné, N. Kamath, F. Crespon, and R. Garcia (2009), Response of the ionosphere to the seismic triggered acoustic waves: Electron density and electromag-

netic fluctuations, *Geophys. J. Int.*, *176*, 1–13, doi:10.1111/j.1365-246X.2008.03818.x.

Link, R., and L. L. Cogger (1988), A reexamination of the O I 6300 Å nightglow, *J. Geophys. Res.*, *93*(A9), 9883–9892.

Liu, J. Y., Y. B. Tsai, K. F. Ma, Y. I. Chen, H. F. Tsai, C. H. Lin, M. Kamogawa, and C. P. Lee (2006), Ionospheric GPS total electron content (TEC) disturbances triggered by the 26 December 2004 Indian Ocean tsunami, *J. Geophys. Res.*, *111*, A05303, doi: 10.1029/2005JA011200.

Lognonné, P., J. Artru, R. Garcia, F. Crespon, V. Ducic, E. Jeansou, G. Occhipinti, J. Helbert, G. Moreaux, and P. Godet (2006), Ground based GPS tomography of ionospheric post-seismic signal, *Planet. Space Sci.*, *54*(5), 528–540, doi:10.1016/j.pss.2005.10.021.

Makela, J. J., B. M. Ledvina, M. C. Kelley, and P. M. Kintner (2004), Analysis of the seasonal variations of equatorial plasma bubble occurrence observed from Haleakala, Hawaii, *Ann. Geophys.*, *22*(9), 3109–3121.

Makela, J. J., M. C. Kelley, and R. T. Tsunoda (2009), Observations of midlatitude ionospheric instabilities generating meter-scale waves at the magnetic equator, *J. Geophys. Res.*, *114*, A01307, doi:10.1029/2007JA012946.

Miller, E. S., J. J. Makela, and M. C. Kelley (2009), Seeding of Equatorial Plasma Depletions by Polarization Electric Fields from Middle Latitudes: Experimental Evidence, *Geophys. Res. Lett.*, *36*(18), L18105, doi:10.1029/2009GL039695.

Najita, K., P. Weaver, and P. Yuen (1974), A tsunami warning system using an ionospheric technique, *P. IEEE*, *62*(5), 563–577.

Occhipinti, G., P. Lognonné, E. A. Kherani, and H. Hébert (2006), Three-dimensional waveform modeling of ionospheric signature induced by the 2004 Sumatra tsunami, *Geophys. Res. Lett.*, *33*, L20104, doi:10.1029/2006GL026865.

Occhipinti, G., E. A. Kherani, and P. Lognonné (2008), Geomagnetic dependence of ionospheric disturbances induced by tsunamigenic internal gravity waves, *Geophys. J. Int.*, *173*(3), 753–755, doi:10.1111/j.1365-246X.2008.03760.x.

Occhipinti, G., P. Coïsson, J. J. Makela, P. Lognonné, E. A. Kherani, and S. Allegeyer (submitted, 2011), Three-dimensional numerical modeling of tsunami-related internal gravity waves in the Hawaiian atmosphere, *Earth Planets Space*.

Peltier, W. R., and C. O. Hines (1976), On the possible detection of tsunamis by a monitoring of the ionosphere, *J. Geophys. Res.*, *81*(12), 1995–2000.

Rolland, L. M., G. Occhipinti, P. Lognonné, and A. Loevenbruck (2010), Ionospheric gravity waves detected offshore Hawaii after tsunamis, *Geophys. Res. Lett.*, *37*(17), L17101, doi:10.1029/2010GL044479.

Wessel, P. (2009), Analysis of observed and predicted tsunami travel times for the Pacific and Indian ocean, *Pure Appl. Geophys.*, *166*(1-2), 301–324, doi:10.1007/978-3-0346-0064-4_15.

Figure 1. Example of 630.0-nm images processed using length-8 FIR filters with passbands of (left) 0.3-1.7 mHz, (middle) 0.3-1.0 mHz to highlight the 26.2-min period waves, and (right) 1.0-1.7 mHz to highlight the 14.2-min period waves. The red line in each image indicates the tsunami location at the time of the image. The green line in the left figure indicates the line from which intensities were taken to construct Figure 2.

Figure 2. Travel-time diagrams for the (top) 630.0-nm emission intensity and (bottom) vertical TEC. The intensities for the top figure were extracted along the green line shown in Figure 1. Structures that are moving at the same speed and direction as the tsunami appear as vertical bands. Negative values along the x-axis indicate structures that appear before the arrival of the tsunami. Both panels are for the respective datasets temporally filtered between 0.3-1.7 mHz.

Figure 3. Comparison of (left) differenced 630.0-nm emission intensity observed at 13:20 and 13:22 UT from Hawaii, (center) electron density at 250 km from a gravity-acoustic model [*Kherani et al.*, 2009], and (right) normalized vertical wind velocity at 250 km from a pure gravity wave model [*Occhipinti et al.*, 2006, 2008, submitted, 2011]. In each case, the red line indicates the tsunami location at the time of the image.

Figure 4. (First panel) Tidal-detrended data (blue line) from DART 51407 and PREM synthetics (red line) centered at the theoretical tsunami arrival time (13:17 UT). (Second panel) Same as the first panel, but zoomed in around the tsunami arrival time. In both panels, the tidal-detrended results are obtained using a least-square fitting over a 45-day time series. The PREM synthetics are computed from source inversion of surface waves in the band 250-450 sec. The synthetics in the first panel are shifted by +0.025 m to allow for a clearer presentation of the data and comparison with the surface waves observed at the DART station about 420 min before the tsunami arrival. (Third panel) Residual sea level variations recorded on DART 51407 filtered from the oceanic tide using high-pass filtering (blue line) or a trend computed from a Fourier model (green line) compared to those using a model based on the co-seismic initial deformation without any precursor signal (red line). The power spectrogram of the data (bottom figure right) indicating a dominant frequency of 0.6 mHz (27.77 min) starting to emerge from the background noise about 20 min prior to the tsunami arrival time. The power spectrogram at the bottom left corresponds to the DART data, with a 5-min cosine taper starting after the tsunami arrival time and with PREM synthetics added before demonstrating that the surface waves are not responsible for generating the long-period waves.

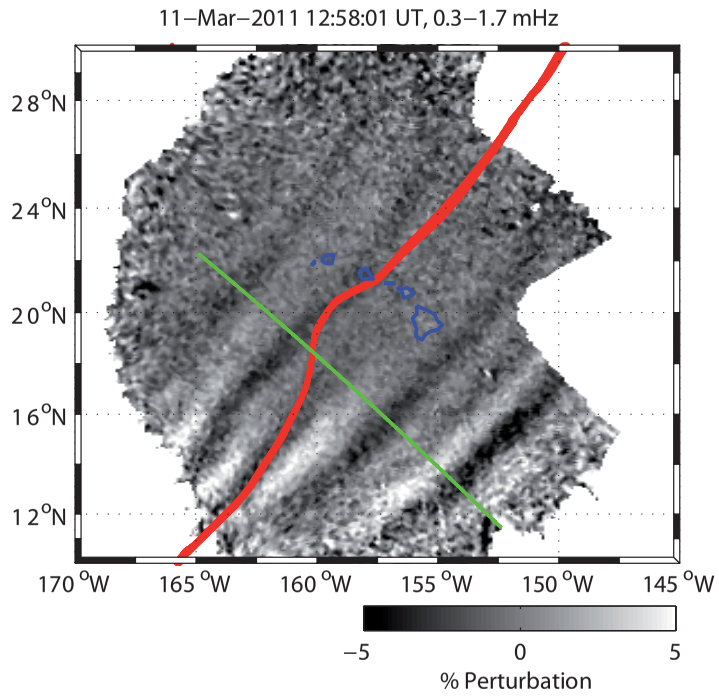
11–Mar–2011 12:58:01 UT, 0.3–1.7 mHz
28°N
24°N
20°N
16°N
12°N
170°W
165°W
160°W
155°W
150°W
145°W
−5
0
5
% Perturbation

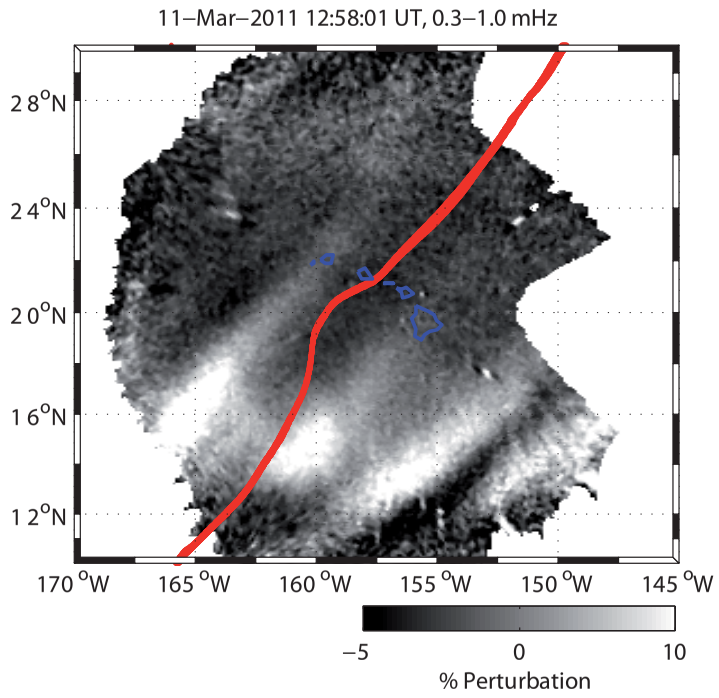
11–Mar–2011 12:58:01 UT, 0.3–1.0 mHz
28°N
24°N
20°N
16°N
12°N
170°W
165°W
160°W
155°W
150°W
145°W
−5
0
10
% Perturbation

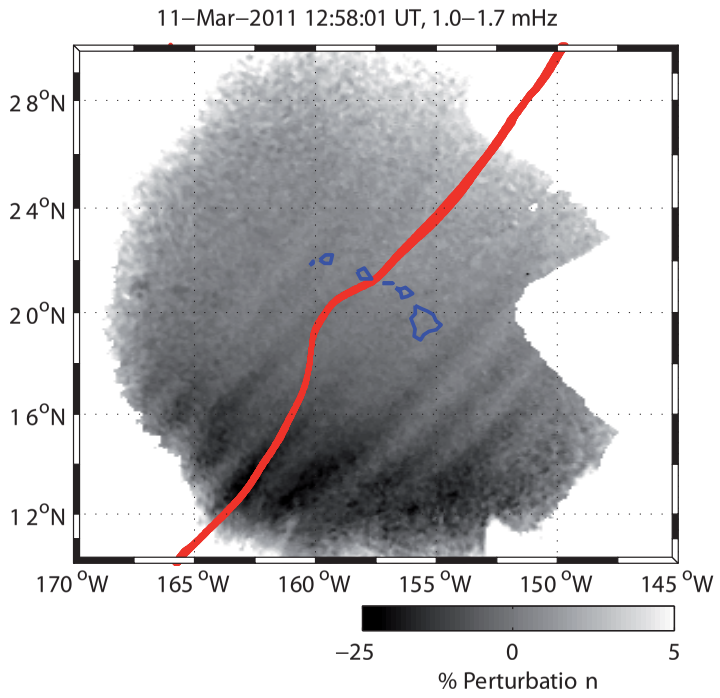
11–Mar–2011 12:58:01 UT, 1.0–1.7 mHz
28°N
24°N
20°N
16°N
12°N
170°W
165°W
160°W
155°W
150°W
145°W
−25
0
5
% Perturbatio n

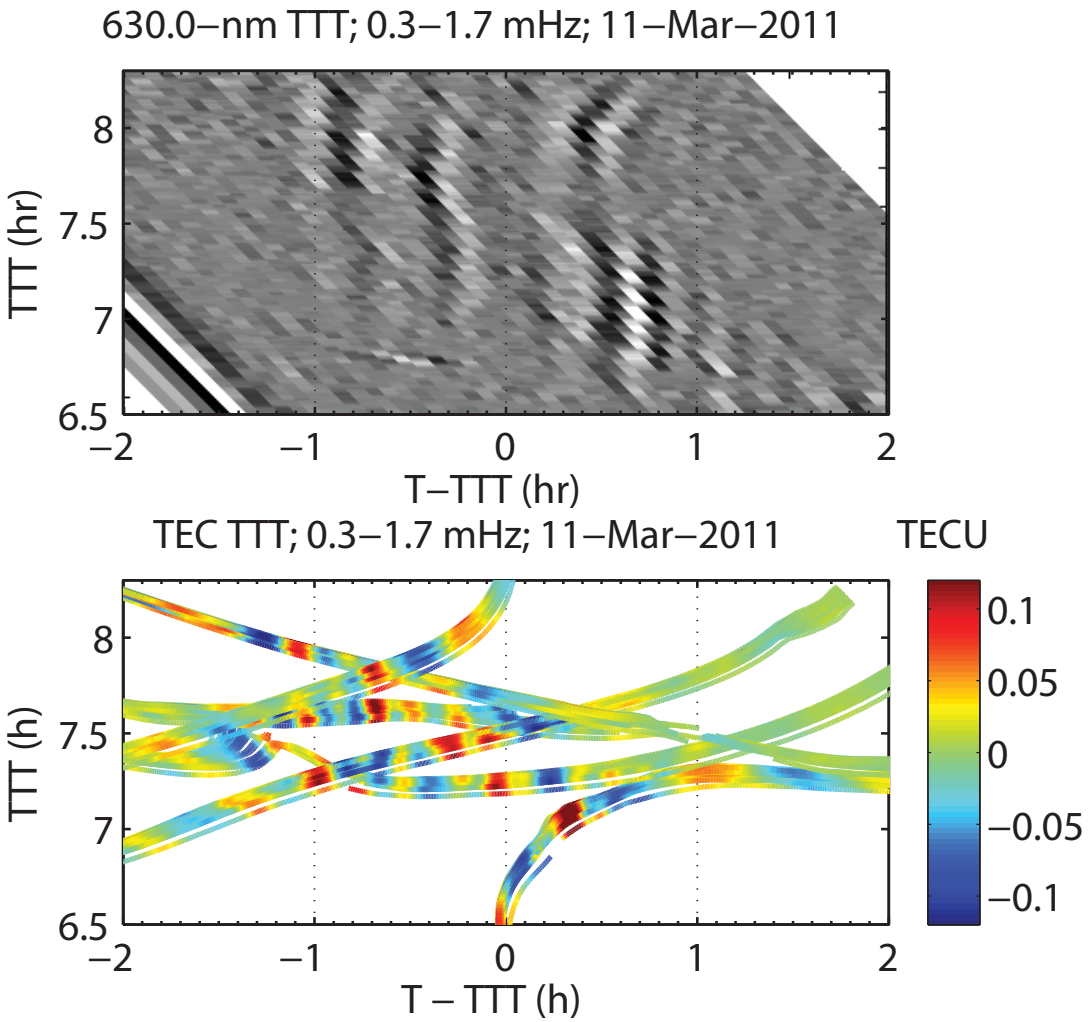
630.0–nm TTT; 0.3–1.7 mHz; 11–Mar–2011
TTT (hr)
8
7.5
7
6.5
–2
–1
0
1
2
T–TTT (hr)
TEC TTT; 0.3–1.7 mHz; 11–Mar–2011
TECU
TTT (h)
8
7.5
7
6.5
–2
–1
0
1
2
T – TTT (h)
0.1
0.05
0
–0.05
–0.1

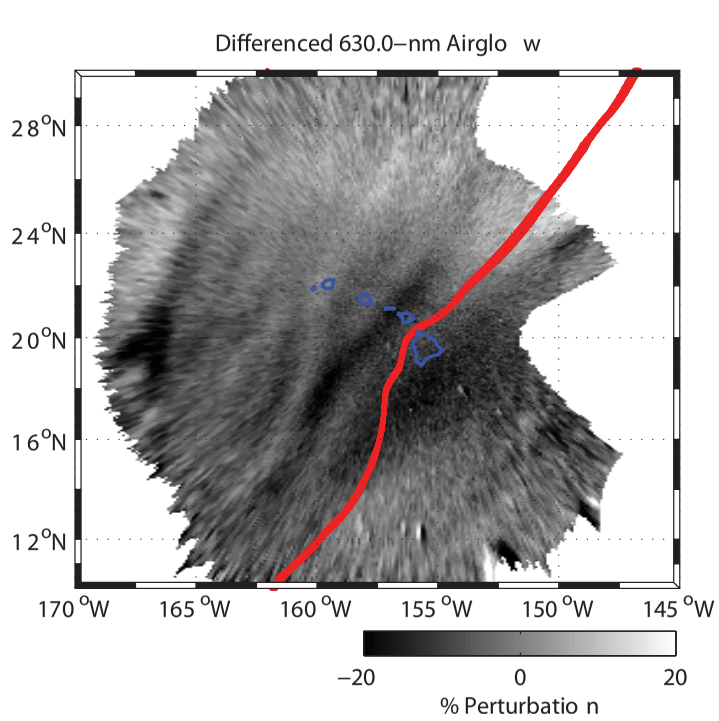
Differenced 630.0–nm Airglo w
28°N
24°N
20°N
16°N
12°N
170°W
165°W
160°W
155°W
150°W
145°W
–20
0
20
% Perturbatio n

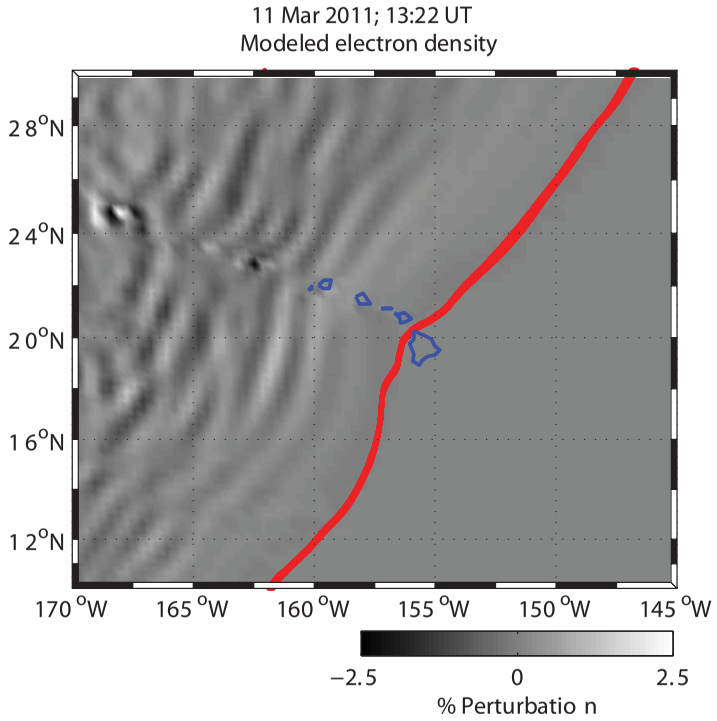
11 Mar 2011; 13:22 UT
Modeled electron density
28°N
24°N
20°N
16°N
12°N
170°W
165°W
160°W
155°W
150°W
145°W
–2.5
0
2.5
% Perturbatio n

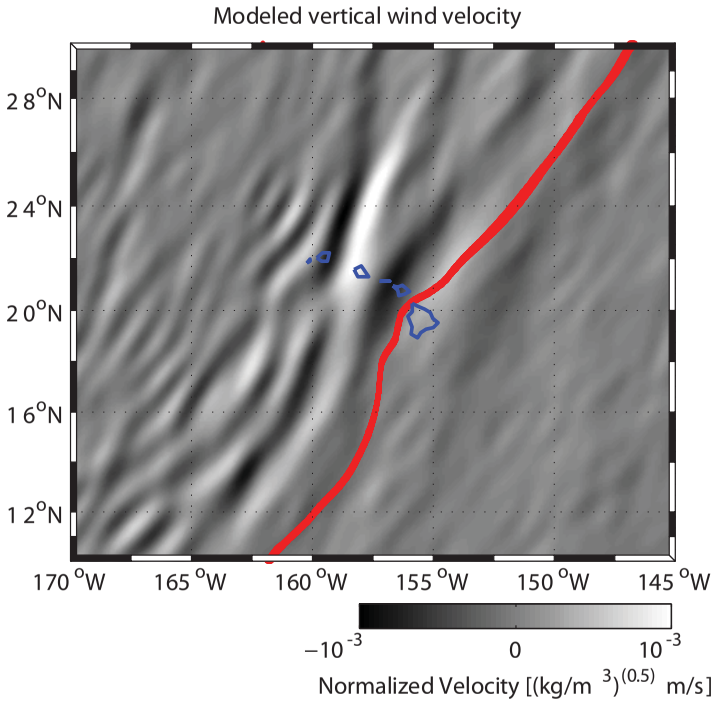
Modeled vertical wind velocity
28°N
24°N
20°N
16°N
12°N
170°W
165°W
160°W
155°W
150°W
145°W
–10^-3
0
10^-3
Normalized Velocity [(kg/m^3)^(0.5) m/s]

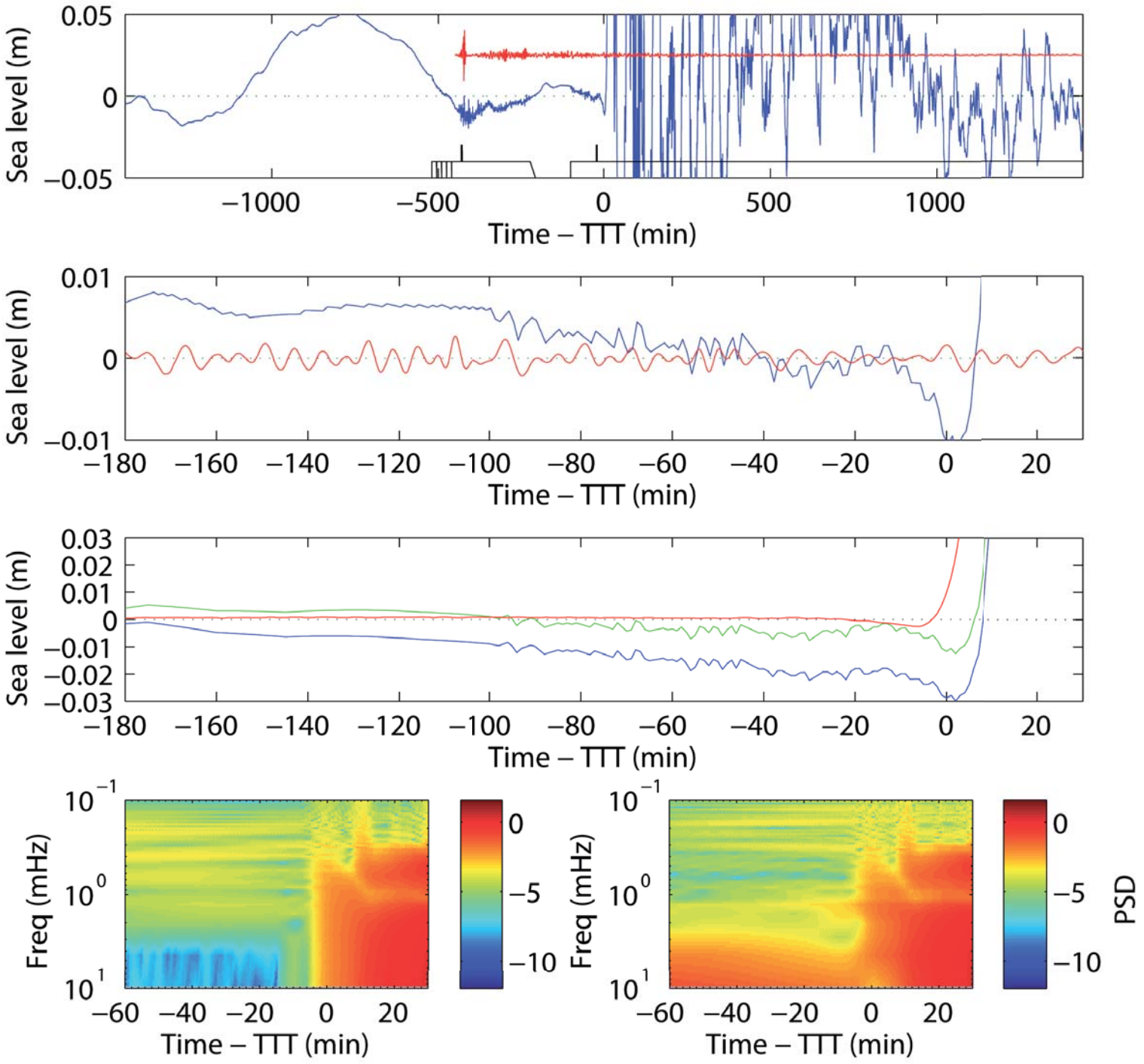
Sea level (m)
0.05
0
−0.05
−1000
−500
0
500
1000
Time – TTT (min)
Sea level (m)
0.01
0
−0.01
−180
−160
−140
−120
−100
−80
−60
−40
−20
0
20
Time – TTT (min)
Sea level (m)
0.03
0.02
0.01
0
−0.01
−0.02
−0.03
Time – TTT (min)
Freq (mHz)
10^{-1}
10^{0}
10^{1}
−60
−40
−20
0
20
Time – TTT (min)
0
−5
−10
Freq (mHz)
PSD